Chemical Engineering Journal 534 (2026) 175063

Contents lists available at ScienceDirect

Chemical Engineering Journal

journal homepage: www.elsevier.com/locate/cej

Electrified catalytic decomposition of methane to hydrogen and carbon nanotubes in Fe-Ni-Co packed bed reactor via magnetic induction heating

Sergey Girshevich [a,b], Stanislav Yakushkin [a,*], Saso Gyergyek [c], Janvit Teržan [a], Anja Sedminek [c], Anej Blažič [a], Elena Sutormina [d], Ilja Gasan Osojnik Črnivec [d], Blaž Likozar [a,*]

[a] National Institute of Chemistry, Hajdrihova 19, Department of Catalysis and Chemical Reaction Engineering, Ljubljana, 1000, Slovenia
[b] University of Maribor, Faculty of Chemistry and Chemical Engineering, Maribor, 2000, Slovenia
[c] Jozef Stefan Institute, Department for Material Synthesis, Jamova Cesta 39, Ljubljana, 1000, Slovenia
[d] National Institute of Chemistry, Laboratory for demonstration of H2 and CO2 technologies, Loke pri Zagorju 14b, 1412, Kisovec, Slovenia

ARTICLE INFO

Keywords:
Catalytic methane decomposition
Hydrogen production
Carbon nanotubes
Magnetic induction heating
Electrification
Metal catalyst

ABSTRACT

For the first time, the experimental feasibility of catalytic methane decomposition (CDM) using magnetically heated catalysts is demonstrated. Magnetic nanoparticles made of iron, nickel, and cobalt alloys were tested for catalytic activity, revealing two distinct carbon formation mechanisms depending on the reaction temperature. Specifically, Ni-Cr-Co and Fe-Ni-Co alloy nanoparticles, as well as Co nanoparticles, were evaluated under magnetic induction heating in the 450–650 °C range. Trimetallic Fe-Ni-Co alloy nanoparticles exhibited the highest stability and CH_4 conversion, reaching >40% at 650 °C. Kinetic studies of the Fe-Ni-Co catalyst revealed no deactivation after 10 h of operation. The magnetic heating regime was shown to be a key factor in catalyst stability, suggesting a unique heat and mass transfer mechanism under magnetic induction heating conditions. The carbon products were analyzed using thermogravimetric analysis, Raman spectroscopy, and electron microscopy. The results revealed that higher operating temperatures favor the formation of less defective graphitic carbon structures. Meanwhile carbon nanotubes, carbon nanofibers, and amorphous carbon are predominantly form at temperatures below 550 °C. Thermogravimetric and Raman analyses confirmed a clear dependence between reaction temperature and the rate of multiwalled carbon nanotube formation. Magnetic induction heating was shown to be a promising approach for catalytic methane decomposition. The use of magnetic heating opens new possibilities for the methane and biogas processing electrification, enabling the production of valuable nanostructured carbon and potentially lowering the cost of bio-based green hydrogen production.

1. Introduction

Continued reliance on fossil fuels as primary energy sources has led to escalating CO_2 emissions, intensifying the global climate crisis and resulting in profound environmental [1], economic [2], and societal consequences [3]. A sustainable transition to carbon-neutral energy carriers is essential, and hydrogen, which produces only water vapor upon combustion, is a particularly promising candidate [4].

Currently, methane is the dominant feedstock for hydrogen production, accounting for nearly two-thirds of global output as of 2024 [5], with steam methane reforming (SMR) remaining the prevailing industrial technology [6]. However, catalytic decomposition of methane (CDM) toward hydrogen and carbon is attracting increasing attention due to its capacity to produce hydrogen without generating carbon dioxide [7].

In addition to its environmental benefits, a techno-economic analysis suggests that CDM could be a cost-effective alternative to SMR, especially if the co-produced carbon can be economically utilized [8].

The viability of CDM hinges on catalyst performance and carbon co-product management [9,10]. For example, carbon nanotubes (CNTs) and carbon nanofibers (CNFs) are valuable material that can be obtained during CDM over specific catalysts [11]. Studies have shown that the type, morphology, and purity of the carbon product depend heavily on the composition of the catalyst and the reaction conditions [8,12]. Xu et al. has shown that larger Ni particles generally favoring CNT/CNF growth while smaller particles favor surface-confined graphitic encapsulation [13].

Recently, the electrification of methane decomposition has emerged

* Corresponding authors.
E-mail addresses: stanislav.iakushkin@ki.si (S. Yakushkin), blaz.likozar@ki.si (B. Likozar).

https://doi.org/10.1016/j.cej.2026.175063
Received 22 September 2025; Received in revised form 27 February 2026; Accepted 8 March 2026
Available online 10 March 2026

as a broader class of hybrid-field catalytic approaches, in which chemical transformations are driven by the combined action of thermal effects and externally applied fields [14]. Such approaches as plasma-assisted, microwave-heated, and magnetically heated catalytic processes have been developed. More broadly, hybrid-field reactor concepts have been recognized as an effective process-intensification strategy, enabling selective and localized energy delivery and functional decoupling of heating and reaction steps across a wide range of catalytic applications [15,16]. A comprehensive review of electrified catalytic methane decomposition, encompassing plasma, microwave, and induction heating strategies, can be found in [17]. Electrified heating methods such as plasma [18–20], microwave [18,21,22], and induction heating [23,24] can all be applied for hydrogen production from methane.

Fulcheri et al. [25] successfully demonstrated plasma methane pyrolysis on a commercial scale for the production of hydrogen and carbon black, achieving 99% methane conversion and 95% hydrogen selectivity. Notably, the reactor operated without a catalyst, and methane decomposition occurred through purely thermal plasma pathways. Wang et al. [19] reported a plasma-catalytic Fe/Al_2O_3 system operating at 700 °C with 42.7% CH_4 conversion, 57.9% H_2 selectivity, and a carbon yield of 105 $mg \bullet g_{cat}^{-1} \bullet h^{-1}$, forming graphitized CNTs. Without catalyst 25% conversion was reached. Cepeda et al. [20] investigated microwave-driven methane pyrolysis at temperatures up to 900 °C and showed that electrode-induced plasma discharges increased CH_4 conversion by up to 20% relative to thermal microwave conditions, producing predominantly nanostructured carbon black.

More recently, microwave-assisted catalytic methane pyrolysis has also been shown to benefit from the formation of conductive carbon nanostructures, which enhance electromagnetic energy coupling and promote methane decomposition kinetics under non-conventional heating conditions. Seyfeli et al. [22] reported methane decomposition over Ni- and Ni-Pd-based catalysts supported on mesoporous carbon and SiC under microwave irradiation, achieving initial hydrogen production rates of 120 $mmol \bullet g_{cat}^{-1} \bullet h^{-1}$ at 500 °C for 15Pd@MC and up to 141 $mmol \bullet g_{cat}^{-1} \bullet h^{-1}$ at 700 °C for 50Ni1Pd@MC, with the formation of nanotube-like and bamboo-shaped carbon structures and improved stability compared to conventional heating. Jiang et al. [26] investigated CNT-supported Ni-Pd and Ni-Cu catalysts at 550–600 °C under microwave and conventional thermal heating. Microwave irradiation enhanced methane conversion rates relative to convective heating, reduced the apparent activation energy from 45.5 to 24.8 $kJ \bullet mol^{-1}$, and enabled a 37% increase in methane conversion rate with only a 10.8% increase in microwave power consumption. Deibel et al. [27] developed a surface-exsolving perovskite ceramic catalyst ($SrTiNi_{0.08}O_3$) for microwave-driven methane pyrolysis, achieving an initial methane conversion of up to 40% together with simultaneous production of CO_x-free hydrogen and carbon nanotubes.

Essyed et al. in a series of works [24,28] demonstrated effective CDM process electrification using induction-heated graphene-coated silica (Zetex), achieving stable methane conversion above 60% at 900 °C, with carbon nanofibers forming as the main carbon product (WTY 3.13 h^{-1}) [28]. It significantly outperformed conventionally heated CDM over the same catalyst, which yielded only 2% conversion.

As illustrated by Lopez-Ruiz et al., one of the most important evaluations of efficient CDM reactor is the energy consumption per hydrogen and carbon production [10]. The most relevant examples of different approaches toward CDM reaction heating could be found in Table S7 with reported CH_4 conversion and carbon production.

Magnetic heating employs ferromagnetic nanoparticles to generate localized heat under an alternating magnetic field. This process offers a new approach to electrified catalysis [29]. Initially applied to organic synthesis [30] magnetic heating has since been extended to gas-phase catalytic reactions [31].

Transition metal nanoparticles based on Ni, Co, and Fe offer a synergistic combination of magnetic and catalytic properties. These ferromagnetic metals are active in CDM process and can be effectively heated in alternating magnetic fields. Furthermore, they are among the few materials that are compatible with CDM's reducing conditions while retaining magnetic responsiveness [31]. For example, Marbaix et al. [32,33] used FeCo alloy nanoparticles as heating agents in propane dry reforming and propane dehydrogenation, achieving reaction temperatures exceeding 600 °C. Although catalytic activity was provided by separate catalytic phases (Ni or Pt-Sn), these studies proved that magnetic heating at high temperatures is feasible.

Magnetically heated catalysts, in which the nanoparticles serve as both the heating agent and the active catalyst have already been used for methane reforming. Almind et al. [34] achieved high (>90%) methane conversions at 800 °C using Co-Ni nanoparticles. Dotsenko et al. [35] showed that the catalytic performance of methane reforming can be adjusted by altering the alloy composition and magnetic field parameters. The authors demonstrated that increasing the Co content can significantly improve the heating properties and, consequently, the methane conversion with fixed inductor power. However, the impact of alloy composition on intrinsic catalytic properties remains to be fully explored.

Nickel, cobalt, and iron have all been investigated as individual CDM catalysts in conventional heating regimes [36]. Gao et al. [37] compared Ni and Co catalysts supported on alumina at 650 °C and reported initial methane conversions of 79.2% and 64.7%, respectively. Ni-based catalysts exhibited superior stability, maintaining over 70% CH_4 conversion after one hour on stream, whereas Co catalysts deactivated rapidly (26.8% CH_4 conversion after one hour on stream). In both cases, CNTs were formed via a base-growth mechanism, with carbon productivities ~0.25 $g_C \bullet g_{cat}^{-1} \bullet h^{-1}$ under the reported conditions.

Fe catalysts have also demonstrated CDM activity and enhanced thermal stability, however, they tend to form lamellar rather than tubular carbon structures [11,39]. According to Pudukudy et al., MgO-supported Fe catalysts produce graphene sheets whereas MgO-supported Ni catalysts produce carbon nanotubes under the same conditions [39]. To increase catalyst stability and selectivity toward CNTs, several researchers have tried bimetallic and trimetallic alloy catalysts based on Fe, Ni, and Co [36,40–44]. For example, Kutteri et al. [38] further demonstrated that the use of bimetallic Ni-Fe and Ni-Co systems under conventional heating can enhance both methane conversion and carbon productivity (up to 2.4 $g_C \bullet g_{cat}^{-1} \bullet h^{-1}$), while enabling controlled CNT formation via both tip- and base-growth pathways.

Using alloyed catalysts composed of Fe, Co, and Ni has the potential to combine their catalytic advantages synergistically and improve overall performance in CDM [36]. Adding Fe into Ni-based systems reduces the formation of encapsulating carbon, and adding Co to Fe-based prevents carbide formation. Both of these factors contribute to enhanced catalyst stability under high-temperature conditions [40,41].

In this study, we demonstrate for the first time the experimental feasibility of magnetic induction heating applied to catalytic methane decomposition using Ni-, Co-, and Fe-based alloy nanoparticles. In this work we report, for the first time, investigation aimed at establishing characteristic trends in catalytic performance, stability, and carbon product formation of CDM process over magnetically heated catalyst. Due to the wide range of compositions and properties, a screening study was performed using unmodified commercial powders to evaluate the materials' catalytic performance, stability, and carbon product characteristics. Pure Ni was excluded due to its low Curie temperature [31]. The results provide new insights into the feasibility of magnetically heated CDM.

2. Experimental

2.1. Materials

The metal alloy nanoparticles were obtained from US Research Nanomaterials, Inc. and Merck for use as a magnetically heated catalyst.

The tested materials included elemental Co, as well as Fe-Ni, Cu-Ni, Fe-Cr-Co, Fe-Ni-Co, Ni-Cr-Co, and Ni-Fe-Cr alloys. All nanopowders have particle sizes below 100 nm. Their key physical properties are summarized in Table S1. To ensure homogeneous bed packing and even temperature distribution, the nanopowders were mechanically mixed with high-purity γ-Al_2O_3 (from Merck) at a fixed weight ratio of 3:7 (metal alloy to alumina). The alumina serves solely as an inert, non-magnetic diluent and does not participate in methane decomposition or inductive heating.

2.1.1. Magnetically heated reactor

We evaluated the prepared catalysts for catalytic methane decomposition (CDM) under magnetic heating conditions. The experimental setup, including the magnetic heating system, followed the configuration described in previous work [45]. A schematic representation of the magnetically heated fixed-bed reactor configuration, including the induction coil, reactor tube, catalyst bed position, and temperature measurement point, is provided in the Supporting Information (Fig. S1).

The setup included an induction coil (Ultraflex HS-4W resonant circuit featuring 0.66 μF capacitors coupled with a 9-turn flat-wound copper tube coil, 17-mm inner diameter, 29-mm outer diameter, 56-mm height operating at a constant 234 kHz) powered by a corresponding SHT-2/400 power supply. The coil was positioned around a fixed-bed quartz reactor tube with a 10-mm inner diameter and a 360-mm length. The magnetic field flux density and frequency were measured by a custom-made probe assembly placed in the center of the induction coil. The induction heater and the coil were cooled by an inner water flow.

For each test the alloy nanopowder, which was diluted with alumina powder, was loaded into the reactor tube. The catalyst bed was secured with quartz wool above and below. The reactor tube was mounted into a stainless-steel housing equipped with a gas inlet, a gas outlet and an internal N-type thermocouple with a diameter of 0.5-mm that was positioned in the center of the catalyst bed. Positioning the thermocouple directly inside the catalyst bed ensures that the reported temperatures correspond to the reaction zone rather than to that of the reactor wall or external housing. The measured temperature therefore provides a direct and reproducible descriptor of the thermal conditions experienced by the catalyst during reaction.

The bed's temperature was continuously monitored, and the induction heater's power was adjusted accordingly to maintain a stable temperature. Several factors beyond the nominal power of the induction coil influence the temperature within the reaction zone, including the material composition, thermal gradient, and magnetic properties of the catalyst bed. Since this study focused on the catalytic performance and long-term stability of the catalysts, all the experiments were carried out at a constant temperature.

To maintain a constant reaction temperature throughout the 10-h tests, an automated control loop was implemented using a custom digital thermocouple data reader based on an Adafruit MAX31856 and an Arduino, combined with a Python script. The induction coil power was dynamically adjusted based on feedback from the internal thermocouple, to ensure thermal stability during the reaction.

All catalytic experiments were conducted at a fixed excitation frequency of 234 kHz, while the magnetic field amplitude was adjusted to maintain the target reaction temperature. The spatial position of the catalyst bed relative to the induction coil was kept constant for all experiments, ensuring reproducible field exposure. Variations in the required magnetic flux density reflect differences in magnetic and thermal properties of the catalyst beds rather than changes in field uniformity.

2.2. Catalyst testing

The steady-state composition of the effluent under isothermal stationary conditions was analyzed using on-line gas chromatography with an Agilent 490 Micro GC equipped with TCD detectors and CP-Molsieve and PoraPlot U columns.

The Micro GC configuration allowed simultaneous quantification of H_2 and CH_4 in the reactor effluent. No CO, CO_2, or higher hydrocarbons were detected under the applied experimental conditions, confirming that methane decomposition proceeded without detectable side reactions.

Prior to each test, the reactor was purged with hydrogen. To evaluate the heating performance and activate the catalysts simultaneously, each catalytic mixture was magnetically heated to 400 °C and calcined at this temperature for 20 min under a hydrogen flow. The results of these preliminary heating evaluations, along with the composition of the metal alloy nanopowder used, are summarized in Table S1.

All catalytic experiments were conducted using a 1 g of catalyst mixture containing 30% of metal alloy nanoparticles, which were diluted with non-magnetic alumina powder. This was done to achieve more even heat distribution, avoid local overheating of the reactor, and provide sufficient bed volume for reliable temperature measurement. As alumina is non-magnetic and catalytically inactive under the investigated conditions, it does not contribute to methane decomposition or heating. Prior to each catalytic test, the reactor was cooled down to room temperature and purged with methane.

Catalytic activity and stability were evaluated over 10 h of continuous operation under a constant flow of pure methane (16 mL/min). For the Ni-Cr-Co catalyst, the maximum temperature achieved under magnetic heating was 450 °C. Accordingly, this catalyst was tested only at that temperature. The remaining catalysts were evaluated at 550 °C.

Methane conversion was calculated based on the difference in concentrations at the inlet and outlet under steady-state conditions. The reaction stoichiometry is provided in Eq. 1.

$$CH_4 \rightarrow 2H_2 + C \tag{1}$$

In our catalytic tests the inlet flow was pure methane and the outlet flow was a mixture of produced hydrogen and unreacted methane. No side products or other gases were detected in the outlet flow.

Then the methane conversion (X_{CH_4}) can be calculated according to Eq. 2.

$$X_{CH_4} = \frac{\frac{1}{2}C_{H_2}^{out}}{0.5 \times C_{H_2}^{out} + C_{CH_4}^{out}} = \frac{C_{H_2}^{out}}{C_{H_2}^{out} + 2 \times C_{CH_4}^{out}} \tag{2}$$

Where $C_{H_2}^{out}$ is hydrogen concentration in the output flow (%), $C_{CH_4}^{out}$ is methane concentration in the output flow (%).

In addition to methane conversion, the catalytic performance was evaluated using normalized reaction rates, hydrogen production rates, and cumulative carbon yields normalized to the mass of active metal. Reaction rates were calculated assuming the stoichiometry $CH_4 \rightarrow C + 2H_2$ and using the known methane inlet flow and metal loading (See Table 1 and Table 2).

Normalized methane decomposition rate in $(\frac{mmol_{CH_4}}{g_{cat} \times h})$

$$r_{CH_4}^n = \frac{v_{CH_4}}{m_{cat} \times t} \tag{3}$$

Was calculated. Where m_{Me} is the mass of active metal in the catalyst bed (g), and t is the reaction time (h).

normalized hydrogen production rate in $(\frac{mmol_{CH_4}}{g_{cat} \times h})$

$$r_{H_2}^n = 2 \times r_{CH_4}^n \tag{4}$$

was calculated assuming the reaction stoichiometry $CH_4 \rightarrow C + 2H_2$,

weight-time yield of carbon in $(\frac{g_C}{g_{cat} \times h})$

$$WTY_c^n = \frac{m_C}{m_{cat} \bullet t} \tag{5}$$

Was calculated. Where m_C (g) is the mass of carbon formed during

Table 1
Catalytic performance comparison of methane decomposition over magnetically heated catalysts.

Reaction temperature, °C	Catalyst	CH_4 conv (0.5 h), %	CH_4 conv, (10*h*), %	Total mass of produced carbon, g	B, mT
550	Co	2.9	1.5	0.078	49
550	Fe-Cr-Co	2.1	2.4	0.083	71
450	Ni-Cr-Co	3.4	9.3	0.4	77
450	Fe-Ni-Co	12.5	7.2	0.38	35
500	Fe-Ni-Co	18.6	14.6	0.7	36
550	Fe-Ni-Co	26.9	21.2	0.94	53
600	Fe-Ni-Co	37.9	32.9	1.41	53
650	Fe-Ni-Co	38.2	41.4	1.78	61

time t (h) and m_{cat} is the mass of active metal in the catalyst bed (g).

Cumulative carbon yield (according to gas conversion measurement) normalized to the mass of active metal in ($\frac{g_c}{g_{cat}}$)

$$C^n_{cum} = \frac{m_C}{m_{cat}} \tag{6}$$

was calculated from the total amount of carbon produced during the entire experiment to mass of active metal in the catalyst bed ratio.

Prior to methane decomposition, all catalysts were subjected to a hydrogen pretreatment at 400 °C under magnetic heating to ensure reduction of the metallic phases. In addition, the strongly reducing reaction environment during methane decomposition further promotes and maintains the metallic state of the active phases, as evidenced by XRD and VSM analyses of the used catalysts.

2.3. Methods

2.3.1. Vibrating sample Magnetometry (VSM)

The magnetic properties of both fresh and used catalysts were evaluated using a vibrating sample magnetometer (VSM, Lake Shore 7400) at room temperature.

2.3.2. X-ray diffraction (XRD)

The phase composition of both fresh and used catalysts was analyzed using X-ray powder diffraction (XRD). Measurements were performed on a PANalytical Empyrean diffractometer equipped with Cu K_α radiation and configured in Bragg-Brentano geometry. The diffraction patterns were recorded at room temperature over a broad 2θ range from 10° to 120°, with a step size of 0.033° and a slow scan rate to ensure high resolution.

Phase identification and structural analysis were carried out using HighScore+ software. Rietveld refinement was applied to the major reflection peaks to extract unit cell parameters.

2.3.3. Chemisorption

Carbon monoxide pulse absorption (CO-PA) was performed on fresh and used materials using the Belcat II analyzer coupled with the BELMASS II-62 quadrupole mass spectrometer (Microtrac, Haan, Nordrhein-Westfalen, Germany). The catalysts were pretreated in a stream of 5 vol % H_2 in Ar (30 ml/min) at 500 °C for one hour. Following pretreatment, the catalysts were exposed to 10 pulses of 5% CO (Messer, purity 5.0) in He. Carbon monoxide absorption was quantified by integrating the mass spectrometer signal at $m/z = 28$ and normalizing it to the catalyst mass.

2.3.4. Thermogravimetric analysis (TGA)

Thermogravimetric analysis (TGA) was performed to evaluate the composition of the used catalysts, with a particular focus on the extent of carbon deposition. Measurements were carried out using a TGA Q5000 instrument (TA Instruments, Inc.). Approximately 13 mg of each sample was heated from approximately 30 °C to 800 °C in air (25 ml/min) at a constant heating rate of 5 °C/min.

To distinguish overlapping processes and enable more accurate interpretation, the TGA curves were converted to their first derivatives and analyzed using Fityk 1.3.1 software [46]. Gaussian functions were fitted to the derivative thermogravimetric (DTG) curves to deconvolute the individual contributions to the overall mass change. This enabled the separation of carbon combustion from metal oxidation processes.

2.3.5. Scanning Electron microscopy with energy dispersive spectroscopy (SEM-EDS)

Surface morphology was examined using a Zeiss Supra 35 VP scanning electron microscope (SEM) equipped with an Oxford Instruments Inca 400 energy-dispersive X-ray spectrometer (EDS). SEM imaging was carried out at an accelerating voltage of 1.00 kV with a 30 μm aperture to capture detailed surface features.

2.3.6. Scanning transmission Electron microscopy (STEM)

The morphology and homogeneity of the catalysts' composition were analyzed using an FTS Talos F200i STEM operated at an accelerating voltage of 200 kV. The samples were ultrasonically dispersed in isopropanol, drop-casted onto copper-supported carbon films and left to dry under ambient conditions. High-angle annular dark-field and bright-field (BF) scanning transmission electron microscopy (STEM) images were acquired simultaneously.

2.3.7. Raman spectroscopy

Raman spectra of the used catalysts were recorded using an Integra Spectra for Materials Science Raman spectrometer (NT-MDT model) equipped with a cooled CCD detector and a 488 nm excitation laser. The spectra were collected at room temperature through a 0.25NA objective over the 872–3500 cm^{-1} range with an average spectral resolution of 1.9 cm^{-1}.

Table 2
Normalized catalytic performance metrics for magnetically heated methane decomposition.

Reaction temperature, °C	Catalyst	CH_4 conv, (10 h), %	$r^n_{CH_4}, \frac{mmol_{CH_4}}{g_{metal} \times h}$	$r^n_{H_2}, \frac{mmol_{CH_4}}{g_{metal} \times h}$	$WTY^n_c, \frac{g_C}{g_{metal} \times h}$	$C^n_{cum}, \frac{g_c}{g_{cat}}$
550	Co	1.5	1.96	3.92	0.03	0.26
550	Fe-Cr-Co	2.4	3.14	6.28	0.03	0.28
450	Ni-Cr-Co	9.3	12.16	24.33	0.12	1.35
450	Fe-Ni-Co	7.2	9.42	18.84	0.13	1.26
500	Fe-Ni-Co	14.6	19.10	38.19	0.23	2.33
550	Fe-Ni-Co	21.2	27.73	55.46	0.31	3.12
600	Fe-Ni-Co	32.9	43.03	86.07	0.47	4.70
650	Fe-Ni-Co	41.4	54.15	108.30	0.60	5.93

3. Results and discussion

3.1. Heating and catalytic tests

In the context of electrified methane decomposition, the performance of magnetically heated catalysts should be interpreted considering the distinct mechanism of energy coupling. Unlike plasma-assisted processes, which rely on non-thermal activation, magnetic induction heating preserves a conventional catalytic reaction pathway, enabling the use of metal-normalized reaction rates and carbon production as intrinsic performance descriptors. At the same time, localized volumetric heating of ferromagnetic catalysts allows high reaction temperatures to be achieved without uniformly heating the reactor walls. In this proof-of-concept study, catalytic performance is therefore discussed in terms of activity trends, stability, and carbon product characteristics rather than direct energy-efficiency benchmarking.

The catalytic performance of the materials under study is presented on Fig. 1(A). All samples, except for the Ni-Cr-Co sample, were tested at 550 °C. The maximum temperature reached for the Ni-Fe-Cr sample was only 450 °C due to this alloy's low Curie temperature; therefore, this catalyst was tested at 450 °C.

As it can be seen in Fig. 1(A) four catalysts were active in methane decomposition; however, conversion was rather low for the Co and Fe-Cr-Co catalysts. In contrast, the Ni-containing catalysts exhibited high methane conversion: 10% for the Ni-Cr-Co at 450 °C and 26% for the Fe-Ni-Co catalyst at 550 °C.

The Ni-Cr-Co catalyst which was tested at a lower temperature (450 °C) initially showed low conversion during the first three hours of the experiment. However, its activity gradually increased, reaching a peak of 10% conversion and stabilizing at 8.4% after 10 h (Fig. 1(I)(c)). Although CDM at such low temperatures is rarely reported in the literature, the performance of the Ni-Cr-Co catalyst at 450 °C is comparable to the best results achieved by Shah et al. [47] for an Al_2O_3 supported Ni catalyst, which reached around 10% methane conversion at 450 °C. Notably, Shah et al. reported fast catalyst deactivation at low temperatures, which did not occur in our experiments. The lag between the start of the reaction and the increase in conversion can be explained by the non-uniform nature of this catalyst, as will be explained later in the STEM section.

The Fe-Ni-Co catalyst exhibited the highest methane conversion rate throughout the entire 10-h test period at 550 °C. After declining from 27% to 21% in the first two hours, the conversion rate stabilized and remained constant until the end of the test (Fig. 1(I)(d)). Importantly, after the initial transient period, no progressive catalyst deactivation was observed under the investigated conditions. The stabilization of methane conversion over extended time on stream indicates a steady-state catalytic regime rather than continuous deactivation.

Throughout the reaction process, the magnetic flux density of the alternating magnetic field in the induction coil was monitored for all the samples. Except for Fe-Cr-Co the initial magnetic flux density required to reach reaction temperature was lower at the end of the experiment than at the beginning (see Fig. S2-S4, Fig.S7).

Initial testing of the Fe-Ni-Co sample at 550 °C revealed exceptionally high catalytic activity. Additional experiments were performed on an Fe-Ni-Co sample at 450 °C, 500 °C, 600 °C, and 650 °C to assess the influence of temperature on catalytic performance, stability, and carbon production. The results of these experiments are summarized in Fig. 1 (II). A consistent pattern was observed in the 450–600 °C range: methane conversion initially increased sharply (up to 38% after 10 min at 600 °C), then declined during the first 2–3 h. After that, a stable plateau was reached (33% after 10 h at 600 °C). The initial and stabilized conversion values both increased with the reaction temperature.

At 650 °C, the catalyst exhibits a similar but even more stable behavior. Methane conversion increased rapidly to 38%, and instead of

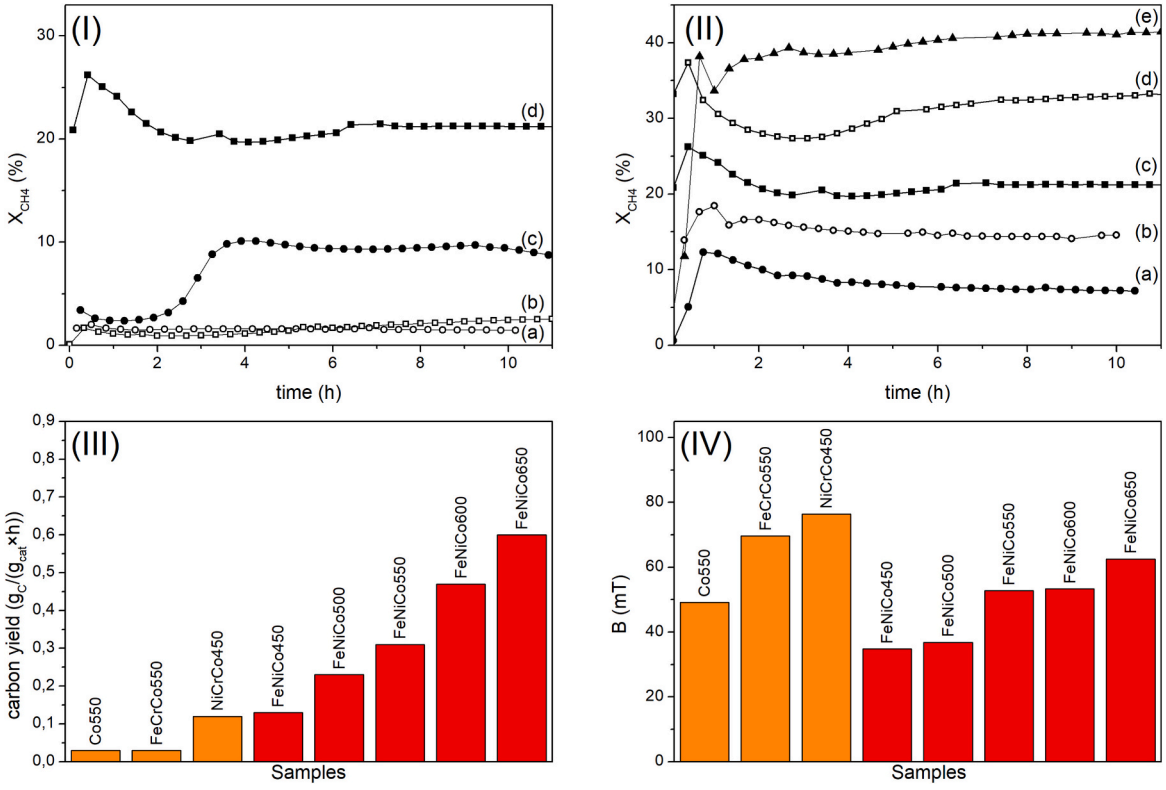

Fig. 1. (I) The catalytic performance of different magnetically heated materials in the CDM reaction at various temperatures is as follows: (a) Co at 550 °C, (b) Fe-Cr-Co at 550 °C (c) Ni-Cr-Co at 450 °C, and (d) Fe-Ni-Co at 550 °C. (II) Catalytic performance of Fe-Ni-Co in the CDM reaction at different temperatures (a) – 450 °C, (b) – 500 °C, (c) – 550 °C, (d) – 600 °C, (e) – 650 °C. (III) Carbon formation rate for all the conducted catalytic tests. (IV) Magnetic flux density required to maintain a stable reaction temperature after 10 h of TOS.

declining, it immediately stabilized and continued to rise gradually, reaching 41% after 10 h. This observation confirms that, within the investigated time-on-stream, the catalyst remains stable under these conditions and does not enter a progressive deactivation regime.

The increase in stabilized methane conversion with temperature observed in this study indicates that, within the investigated time-on-stream, the catalyst does not enter a progressive deactivation regime. One possible explanation for this behavior is related to the magnetic induction heating mechanism. Unlike conventional external heating, magnetic heating provides localized energy input directly to ferromagnetic catalyst particles, which may influence carbon growth dynamics and catalyst-carbon interactions, potentially delaying catalyst deactivation.

At the same time previous studies have demonstrated that catalyst stability in methane decomposition is highly sensitive to catalyst formulation. For example, as summarized by Hantoko et al. [48] based on experimental studies by Bayat et al. [40,49], the transition from mono- to bi- and trimetallic Ni-based catalysts under otherwise identical reaction conditions resulted in substantially improved catalyst stability. In particular, while monometallic Ni catalysts exhibited rapid deactivation and bimetallic Ni-Fe catalysts showed onset of deactivation after approximately 5 h time-on-stream, trimetallic catalysts (Ni-Fe-Cu) maintained stable methane conversion without detectable deactivation over at least 10 h time-on-stream.

The magnetic flux density required to maintain a stable temperature is directly proportional to that temperature (see Table1–2 and Fig. S10). For all experiments conducted at temperatures higher than 450 °C the required field strength decreased throughout the experiment.

Using the conversion dependency from time, we calculate the average carbon weight-time yield over the duration of each experiment (Fig. 1(III)). The lowest carbon yields were observed for the Ni-free catalysts: (0.03 $g_c \bullet g_{cat}^{-1} \bullet h^{-1}$ for Co at 550 °C). The Fe-Ni-Co catalyst produced the highest overall carbon production, with values consistently increasing with reaction temperature: from 0.13 $g_C \bullet g_{cat}^{-1} \bullet h^{-1}$ at 450 °C, to 0.6 $g_C \bullet g_{cat}^{-1} \bullet h^{-1}$ at 650 °C.

Direct, one-to-one comparison of methane conversion across catalytic methane decomposition studies is complicated by differences in catalyst formulation (mono-, bi-, and tri-metallic systems), metal loading and dispersion, reactor configuration, and space velocity. In addition, many conventionally heated CDM studies operate at temperatures of 650–700 °C or higher, whereas the present proof-of-concept screening focuses on tri-metallic Fe-Ni-Co catalysts in the lower temperature range of 450–650 °C using unmodified commercial alloy powders.

Within the available literature, the most relevant references for benchmarking are the works of Al-Fatesh et al. [44] and Kutteri et al. [38]. Al-Fatesh et al. investigated alumina-supported Fe-Ni-Co catalysts prepared by wet impregnation under conventional external heating and reported stable methane conversions of 65–70% over 3 h time-on-stream at 700 °C, with substantially lower conversions at 650 °C with metal loading 0.3 g and GHSV 5000 $ml \bullet g_{cat}^{-1} \bullet h^{-1}$. Kutteri et al. reported methane conversions on the order of 55–60% at 650 °C over Ni-rich bimetallic catalysts with 0.1 g of catalyst loading and GHSV 12600 $ml \bullet g_{cat}^{-1} \bullet h^{-1}$, under conventional heating, albeit demonstrated over relatively short time-on-stream ($\leq$1 h).

In the present work, the magnetically heated Fe-Ni-Co catalyst reaches a stable methane conversion of 41% at 650 °C after 10 h on stream. Taken together, these comparisons indicate that magnetic induction heating enables catalytic methane decomposition performance within the range reported for conventionally heated transition-metal catalysts at comparable temperatures.

Methane conversion trends show catalyst stability and temperature trends. To compare intrinsic catalytic performance with results reported in the literature, normalized reaction rates, hydrogen production rates, and carbon weight-time yields for studied catalysts are reported in (Table 2).

3.2. XRD

XRD diffraction patterns were analyzed for all the samples under study, both fresh and used. The crystallite size, corresponding to coherent diffraction domains and derived from the Scherrer equation, was found to be in the range of 40–100 nm for all the samples (Table S3). The Ni-Cr-Co sample did not show evidence of a Cr-containing phase, which aligns with the EDS result indicating a high oxygen content and non-uniform phase composition of the particles in this sample. The metallic phase diffraction peaks shifted slightly and narrowed after the reaction, which can be interpreted as an increase in crystalline size due to particle reduction and sintering at higher temperatures (Fig. 2, Table S3). These XRD-derived crystallite sizes reflect coherent diffraction domains and may differ from the apparent particle dimensions observed by electron microscopy, where agglomeration and carbon overgrowth can contribute to larger apparent sizes.

After 10 h of operation, a distinct peak associated with graphitic carbon is detected in diffraction patterns of the Ni-Cr-Co and Fe-Ni-Co catalysts. This reflection appears at 26.3°, which is consistent with the assignment to graphitic carbon reported by Bayat et al. [40,41] and corresponds to the standard [JCPDS No. 01–0640]. For the Fe-Ni-Co samples treated at different temperatures, the intensity of this peak increased with reaction temperature, indicating carbon accumulation (see Fig. 2), which is in accordance with the results of the catalytic tests.

3.3. VSM

VSM measurements confirmed that all fresh and used samples exhibited ferromagnetic behavior, regardless of their composition. The hysteresis loops of all the samples are inclined, reflecting the superparamagnetic behavior of the nanoparticles in the samples. Notably, while the hysteresis loop is closed at $B = 1$ T, the magnetization curve is not horizontal. To facilitate interpretation, theoretical saturation magnetization (M_S) values were calculated based on the weighted contributions of the metallic components relative to the alumina content [50]. For the used samples, these values are influenced also by carbon deposition. The presence of this nonmagnetic carbon phase led to a uniform decrease in M_S for all used materials. The fresh Co sample showed a pronounced discrepancy between the theoretical and experimental M_S, indicating cobalt's nanoparticles tendency to oxidize [51]. STEM analysis confirms this, detecting an oxide shell around the Co particles (Fig. S21). Interestingly, the used Co sample exhibited an increase in M_S (Fig. 3(A)), suggesting partial re-reduction of the oxidized Co nanoparticles under the CDM reaction conditions. In the case of Ni-Cr-Co, the overall M_S was significantly lower (Fig. 3(B)). Given the known low magnetic response of CrNi alloys, the measured M_S is primarily attributed to the Co phase [52,53]. The Fe-Ni-Co catalyst exhibited the highest M_S. Increasing the reaction temperature leads to a higher carbon content in the used samples, consequently resulting in a lower detected M_S value (Fig. 3(C)).

The results of the TGA study were used to account for the dilution of the magnetic material in the used samples with the carbon products. The theoretical M_S values were corrected for carbon deposition, as determined by TGA (see Section 3.5), and are presented in Table S5. The difference between the calculated and experimental saturation magnetization values is much lower for the used samples. This is probably due to the reductive nature of the reaction medium and the formation of a graphitic protective layer, which suppresses further oxidation of the metal nanoparticles after the reaction. These results align well with those of the chemisorption study (see Section 3.4).

3.4. Chemisorption

A significant decrease in CO uptake was observed in the used Fe-Ni-Co-based catalysts compared to the fresh one, indicating a progressive blocking of the active sites by deposited carbon. The extent of blocking

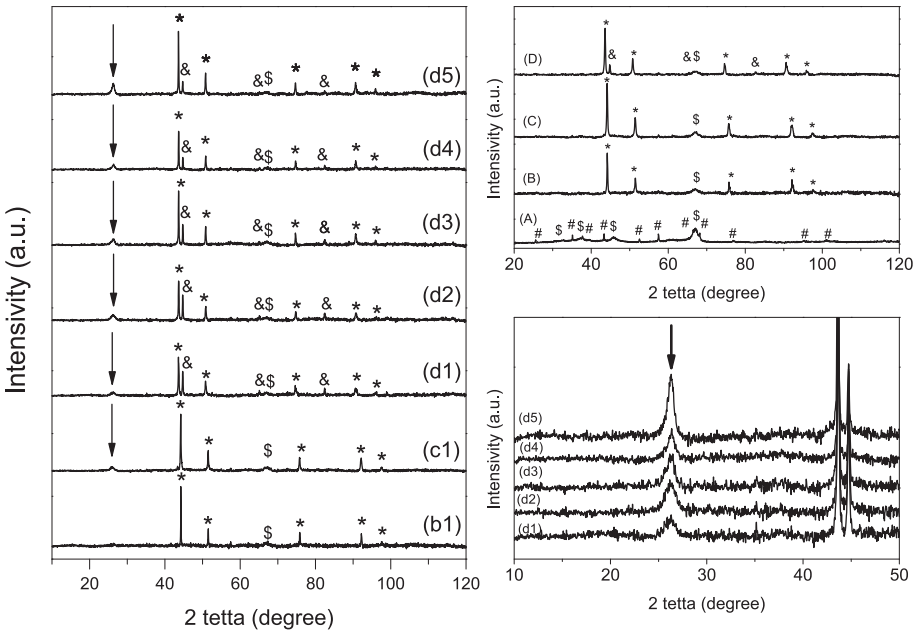

Fig. 2. XRD patterns of fresh and used samples: (A) γ-Al_2O_3 support, (B) fresh Co sample, (C) fresh Ni-Cr-Co sample, (D) fresh Fe-Ni-Co sample. Used catalysts after 10 h of operation: (a1) Co at 550 °C, (b1) Ni-Cr-Co at 450 °C, and Fe-Ni-Co samples treated at different temperatures ((d1) 450 °C, (d2) 500 °C, (d3) 550 °C, (d4) 600 °C, (d5) 650 °C).
Phase assignments: $ - γ-Al_2O_3, # - α-Al_2O_3, * - Ni/Co alloy phase, & - Fe alloy phase, ↓ - carbon.

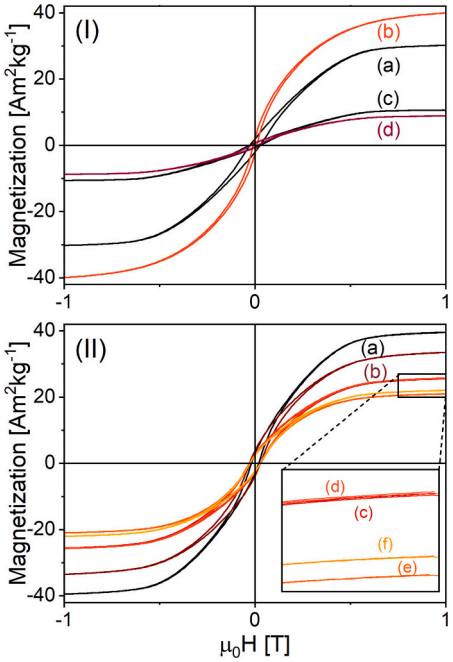

Fig. 3. Room-temperature magnetic hysteresis loops for fresh and used (10 h TOS) catalysts indicated on the plot: (I) (a) Co fresh, (b) Co after 550 °C; (c) Ni-Cr-Co fresh, (d) Ni-Cr-Co after 450 °C; (II) Fe-Ni-Co: (a) – fresh, (b) – after 450 °C, (c) – 500 °C, (d) – 550 °C, (e) – 600 °C, (f) – 650 °C.

correlated strongly with the reaction temperature. After operation at 450 °C, 19% of the active surface was blocked; after operation at 500 °C, 59% was blocked; and after operation at 550 °C and above, over 90% was blocked. Due to the nature of the measurement and the small amounts of adsorption, it can be assumed that all of the metal was covered in carbon when the reaction proceeded at temperatures above 550 °C (see Table 3).

Table 3
Results of CO chemisorption tests for fresh and used Fe-Ni-Co catalysts.

Condition	N (CO), mmol/g	C covered metal, %
Fresh	$2.85•10^{-3}$	0
Used after 10 h at 450 °C	$2.32•10^{-3}$	19
Used after 10 h at 500 °C	$1.16•10^{-3}$	59
Used after 10 h at 550 °C	$2.77•10^{-4}$	90
Used after 10 h at 600 °C	$1.74•10^{-4}$	93
Used after 10 h at 650 °C	$5.71•10^{-5}$	98

At lower temperatures, the relatively low CO adsorption indicates that the carbon is deposited primarily in an amorphous or nano-structured form. This carbon species are located around the particle without completely passivating it. In contrast, the nearly complete suppression of CO chemisorption at higher temperatures reflects the formation of encapsulating carbon layers that encapsulate and isolate the metallic sites from the gas phase.

Interestingly, despite nearly complete blocking of the metallic nanoparticles by carbon at higher temperatures, no significant decrease in methane conversion was observed during the reaction. This suggests that methane molecules can still access metallic active sites despite the presence of a carbon overlayer, potentially via diffusion through defects or grain boundaries in the graphitic shell. While carbon materials have been reported to catalyze methane decomposition at substantially higher temperatures [48], the contribution of the carbon layer itself to methane activation under the present reaction conditions is expected to be limited.

3.5. TGA

Thermogravimetric analysis (TGA) was performed on used samples that exhibited measurable carbon accumulation, namely the Fe-Ni-Co and Ni-Cr-Co catalysts (Fig. 4(A)). At identical reaction temperatures, both catalysts showed comparable total mass loss associated with carbon oxidation. The apparent differences between them arise from the wider range of reaction temperatures investigated for Fe-Ni-Co (450–650 °C), whereas Ni-Cr-Co was evaluated only at 450 °C. Therefore, the similar

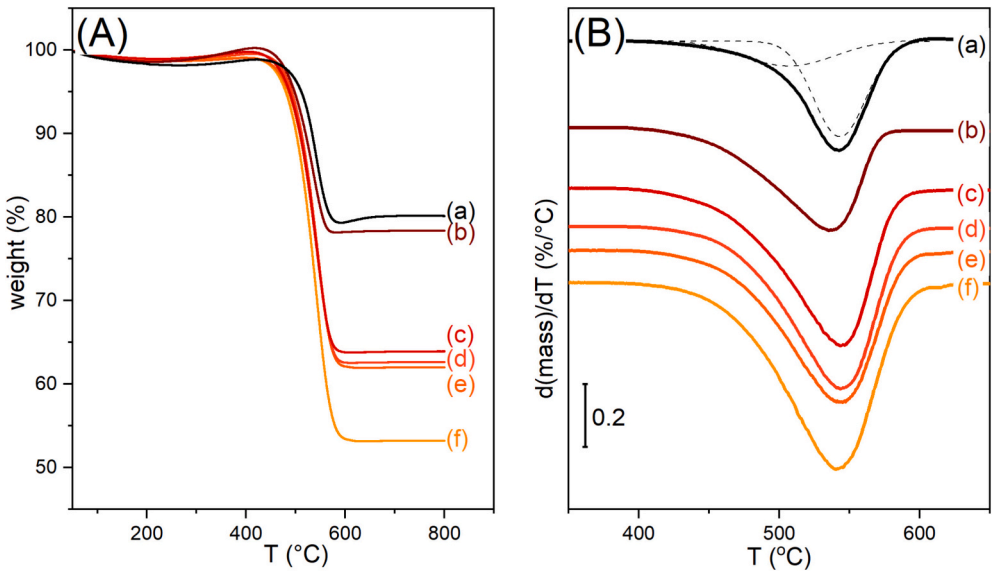

Fig. 4. (A) Thermogravimetric analysis and (B) derivative thermogravimetric (DTG) curves of used catalysts with varying compositions and operating temperatures (a) – Ni-Cr-Co after 450 °C; (b) – Fe-Ni-Co after 450 °C; (c) – Fe-Ni-Co after 500 °C; (d) – Fe-Ni-Co after 550 °C; (e) – Fe-Ni-Co after 600 °C; (f) – Fe-Ni-Co after 650 °C.

mass losses observed at the same operating temperature indicate that both catalysts form comparable amounts of carbon under equivalent conditions. A small initial mass loss below ~200 °C is attributed to desorption of physically adsorbed moisture and weakly bound surface species. Upon further heating in the oxidative TGA atmosphere, partial oxidation of reduced Fe/Ni/Co metallic phases to their corresponding oxides leads to a compensating mass gain, resulting in an apparent recovery of the sample mass prior to carbon oxidation.

The DTG curves reveal nonsymmetric oxidation profiles characteristic of carbon species with different degrees of structural order. The oxidation of disordered or amorphous carbon begins between approximately 350 and 400 °C, while more ordered species, such as filamentous carbon or carbon nanotubes, oxidize predominantly in the 500–600 °C range. This interpretation is consistent with prior reports that associate higher oxidation temperatures with carbon of increasing structural order [44,54–56].

Similar two-step oxidation behavior has been reported by Bayat et al. [40,41], who studied CDM over Ni-Fe/Al_2O_3 and Ni-Fe-Cu/Al_2O_3 catalysts. In their work, the low-temperature oxidation peak was attributed to encapsulating carbon, whereas the high-temperature peak was assigned to more ordered nanostructured carbon, including carbon nanofibers (CNFs) and nanotubes (CNTs). Increasing the reaction temperature shifted the high-temperature oxidation peak to higher oxidation temperatures on the temperature programmed oxidation curve, indicating progressive structural ordering of the carbon phase.

A comparable behavior is observed in our system. For both catalysts, two oxidation peaks are detected and can be reasonably assigned to encapsulating carbon (low-temperature peak) and nanostructured carbon (high-temperature peak). A shift of both oxidation peaks toward higher oxidation temperatures is evident when the reaction temperature is increased from 450 to 550 °C; for the samples after the reaction at temperatures above 550 °C, the peak positions remain essentially unchanged.

A quantitative comparison further highlights the difference between the two catalysts. For Ni-Cr-Co, operated at 450 °C, the ratio of the low-temperature to the high-temperature oxidation peak is 0.56, whereas for Fe-Ni-Co at the same temperature this ratio is 1.45. This substantial difference indicates that Ni-Cr-Co produces a larger relative fraction of nanostructured carbon (CNFs, CNTs), while Fe-Ni-Co forms predominantly encapsulating carbon under identical reaction conditions (Table S4).

A further internal consistency can be noted when comparing the evolution of the low-temperature TGA fraction for the Fe-Ni-Co catalyst with independent chemisorption measurements. The relative area of the low-temperature oxidation peak increases from 14% to 24% (Table S4) as the reaction temperature, is raised from 450 to 650 °C, while the surface carbon saturation determined by CO chemisorption increases in a similar manner, from 18% to 98% (Table 3). Since the low-temperature TGA feature is associated with encapsulating carbon, this parallel trend supports the interpretation that progressive accumulation of surface-bound carbon reduces the accessibility of metallic sites.

When comparing these TGA-derived values with the expected relationship from methane conversion kinetics, a discrepancy becomes apparent at elevated reaction temperatures. According to the kinetic formulation, the integral CH_4 conversion should be directly proportional to the total amount of carbon formed. However, the TGA measurements show lower apparent carbon accumulation at higher temperatures, particularly for the Fe-Ni-Co catalyst after operation at 600 and 650 °C. This observation may indicate that, at elevated temperatures, a fraction of the formed carbon does not remain permanently attached to the catalyst bed and may be transported downstream, leading to an underestimation of total carbon formation when based solely on recovered solids. These mobile carbon species would escape collection during reactor disassembly and thus remain undetected by solid-phase analytical methods (see Table 4).

In conventionally heated catalytic methane decomposition, the type

Table 4
Carbon mass balance and distribution of carbon types in used catalysts operated at different temperatures.

Used catalyst	Ni-Cr-Co	Fe-Ni-Co				
Operating temperature, °C	450	450	500	550	600	650
Calculated carbon accumulation according to CH_4 conversion, g	0.40	0.38	0.70	0.94	1.42	1.78
Calculated carbon accumulation according to TGA, g	0.26	0.39	0.81	0.91	0.72	1.13

and stability of carbon products are known to depend strongly on catalyst composition, metal-support interaction, and reaction temperature. Kutteri et al. [38] investigated methane decomposition over mono- and bimetallic 3d transition metal catalysts (including Fe-Ni systems) at temperatures around 650 °C and reported the formation of carbon nanotubes via both tip- and base-growth mechanisms. In their work, catalyst deactivation was closely linked to the balance between filamentous carbon growth and surface-confined encapsulating carbon, with excessive encapsulation leading to loss of activity.

In comparison, the present Fe-Ni-Co system exhibits different behavior, likely linked to the use of magnetic heating method. Despite the progressive accumulation of encapsulating carbon at elevated temperatures, no corresponding decline in methane conversion is observed over 10 h time-on-stream.

3.6. SEM and STEM analysis

In addition to qualitative imaging, particle-level metal compositions were examined by STEM-EDS. For the Fe-Ni-Co catalyst, the particle-level composition ranges are consistent with the nominal alloy composition and with the phase information obtained from XRD refinement, whereas the Ni-Cr-Co catalyst shows clear phase segregation into Co-

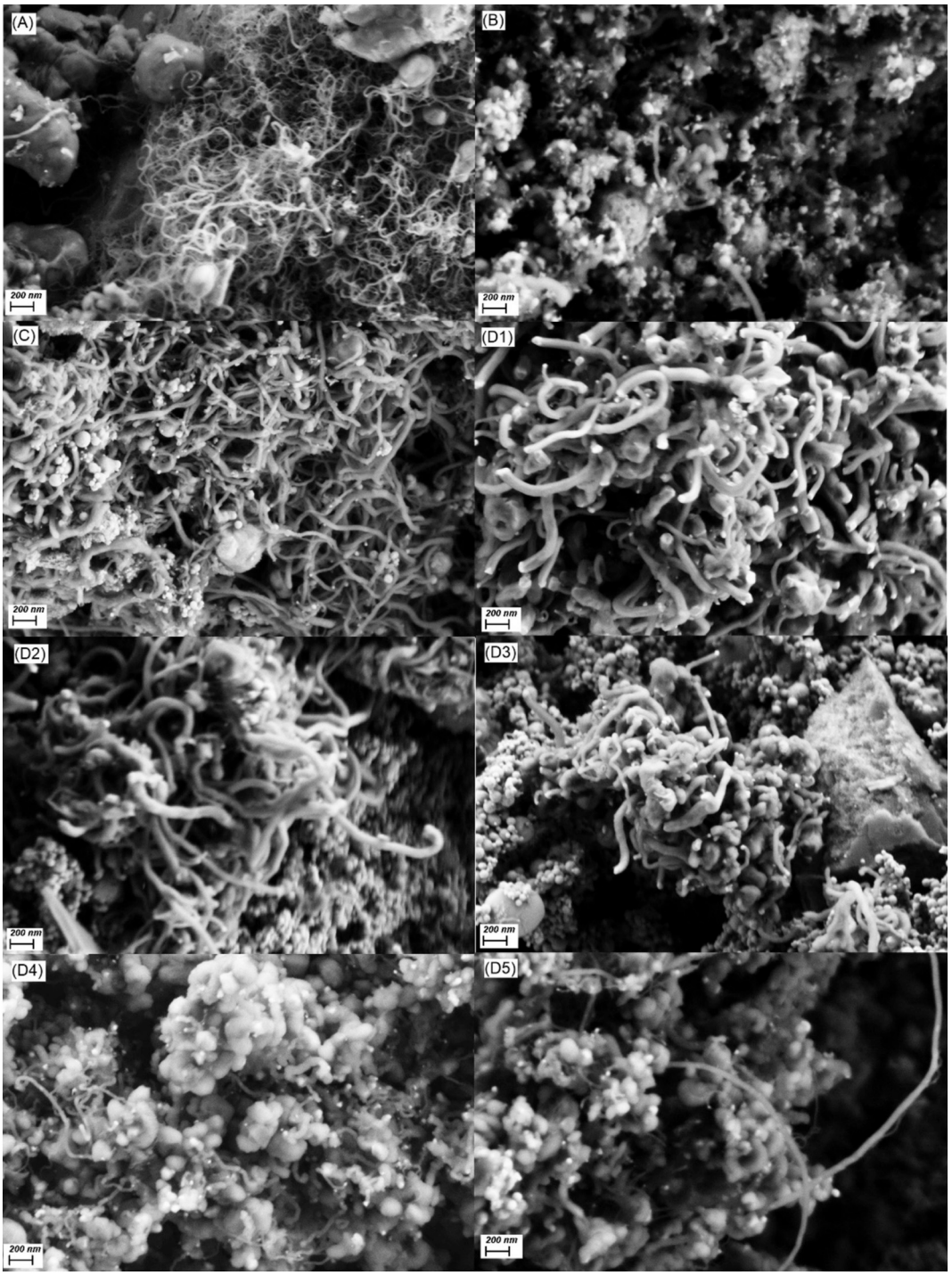

Fig. 5. SEM images of catalysts after 10 h of methane decomposition. (A) Co at 450 °C; (B) Fe-Cr-Co at 600 °C; (C) Ni-Cr-Co at 450 °C; (D1–D5) Fe-Ni-Co at (D1) 450 °C, (D2) 500 °C, (D3) 550 °C, (D4) 600 °C, and (D5) 650 °C, illustrating the evolution of carbon morphology with reaction temperature.

rich and Cr-Ni-rich components. Detailed STEM-EDS quantification and representative composition ranges are provided in the Supporting Information (Table S2).

The morphology of the carbon products formed during methane decomposition was examined using SEM and STEM imaging of the used catalysts after 10 h time-on-stream (Fig. 2(A)–(D)). Different magnifications were employed to capture both global carbon morphology and local particle-carbon interfacial features. Distinct differences in carbon structure were observed as a function of catalyst composition and reaction temperature. Fig. 5(A–C) illustrates morphology differences between catalyst compositions, while Fig. 5(D1–D5) shows the temperature-dependent evolution of carbon morphology for the Fe-Ni-Co catalyst. Metal nanoparticles were frequently observed at the tips of the carbon nanotubes (CNTs) in all samples (Fig. S13–S20), indicating that CNT growth predominantly proceeds through a tip-growth mechanism. This aligns well with the nature of the sample, consisting of unsupported metal alloy nanoparticles [37,57,58].

Qualitative SEM analysis reveals clear differences in filament morphology between the catalyst with different composition at the same operating temperature. At 450 °C, the Fe-Ni-Co catalyst (Fig. 5(D1)) forms relatively thick carbon filaments with apparent diameters of approximately 60–70 nm (Fig. S16), whereas the Ni-Cr-Co (Fig. 5(C)) catalyst produces thinner nanostructures of roughly 40–50 nm (Fig. S14). The Co-based catalyst forms very narrow, densely interwoven carbon deposits (Fig. 5(A)) with diameters on the order of 20–25 nm (Fig. S13), despite its low methane conversion, while the Fe-Cr-Co catalyst yields comparatively sparse and thicker filaments (Fig. 5(B)). These observations highlight that catalyst composition strongly influences the texture and size of the resulting carbon products. As SEM is inherently qualitative, the diameter values should be regarded as approximate; nevertheless, the trends are reproducible across multiple imaging regions.

For the Fe-Ni-Co catalyst, filamentous carbon forms across the entire investigated temperature range (450–650 °C). At 450 °C, the filaments appear relatively thick and curved, while with increasing reaction temperature they become thinner and more uniform (Fig. 5(D1–5)), which aligns with results reported in literature [40]. At higher temperatures, a broad distribution of filament diameters is observed, without a clear dominant size, which reflects the increasing diversity of carbon morphologies formed under these conditions (Fig. 5(D2–5)).

At 600 °C, dense graphitic deposits increasingly cover the catalyst surface (Fig. S12(E1)), consistent with a transition from predominantly filamentous growth to surface-confined graphitic deposition. Such deposition is characteristic of progressive encapsulation of metallic nanoparticles, which suppresses filament elongation and favors the development of graphitic layers.

EDS mapping (Fig. 6(C)) shows that at lower reaction temperatures, carbon primarily accumulates at the edges of nanoparticle agglomerates, leaving much of the metal surface accessible. At higher temperatures, continuous graphitic layers form directly on the surface of the nanoparticles (Fig. 6(D)). This confirms that, under these conditions, at least two distinct types of carbon structures are present simultaneously.

Transmission electron microscopy (TEM) was employed to further examine the nanoscale morphology of the carbon structures formed over the Fe-Ni-Co catalyst at 600 °C. The TEM images reveal multi-walled carbon nanotubes with well-defined walls, together with concentric graphitic carbon layers partially or fully encapsulating individual metallic nanoparticles. Such coexistence of filamentous carbon and surface-confined graphitic layers suggests the operation of competing carbon growth pathways. Similar behavior has been mechanistically rationalized in thermocatalytic methane decomposition, where carbon formation proceeds via competition between surface C-C coupling leading to graphitic encapsulation and diffusion of atomic carbon into the metal sublayer enabling CNT or CNF growth [59]. These observations provide direct structural evidence that surface-confined graphitic deposition occurs in parallel with nanotube growth (see Fig. 7).

Overall, electron microscopy analysis demonstrates that all catalysts produce carbon nanostructures across the studied temperature range. For the Fe-Ni-Co catalyst, filamentous carbon is observed from 450 °C onward, while at higher temperatures the coexistence of carbon

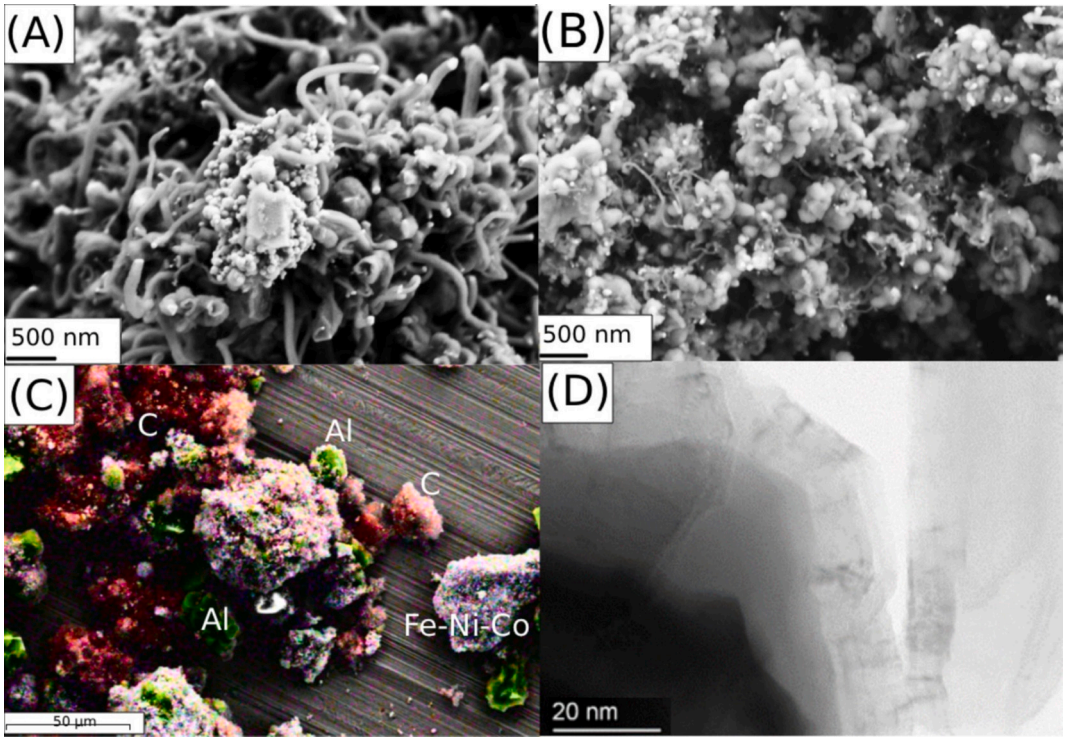

Fig. 6. SEM-EDS images (A–C) and STEM image (D) of used catalysts after 10 h of methane decomposition. (A) Fe-Ni-Co after 450 °C (B) Fe-Ni-Co after 600 °C; (C) Fe-Ni-Co after 450 °C EDS mapping. The elements are marked on the image. (D) STEM images of Fe-Ni-Co catalyst after operation at 600 °C.

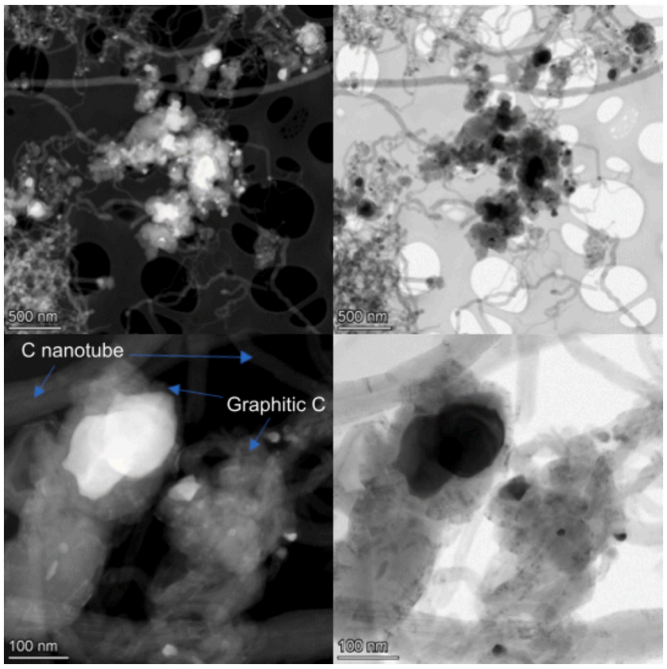

Fig. 7. TEM images of used Fe-Ni-Co catalyst after 10 h of methane decomposition at 600 °C, showing the coexistence of multi-walled carbon nanotubes and graphitic carbon shells encapsulating metallic nanoparticles. Arrows indicate representative nanotube structures and graphitic carbon layers.

nanotubes and surface-confined graphitic layers indicates that multiple carbon growth modes operate simultaneously under magnetic induction heating.

3.7. Raman spectroscopy

Raman spectroscopy was used to investigate the structure and disorder of carbon deposited on used catalysts. All samples exhibited the characteristic D (~1356–1359 cm^{-1}), G (~1575–1582 cm^{-1}), and 2D (~2696–2710 cm^{-1}) bands, commonly associated with sp^2-hybridized carbon. The D band reflects the presence of structural defects and disorder, and the G band indicates graphitic order (Fig. 8). The 2D band provides additional information on the degree of graphitization and the number of graphene layers (see Table 5).

Spectra deconvolution revealed additional contributions from bands such as D′ (~1610 cm^{-1}), D3 (~1495 cm^{-1}), and D″ (~1125 cm^{-1}), which are associated with edge defects, amorphous carbon, and possible oxygen-containing species, respectively (see ESI). Defective or amorphous carbon formation was especially prominent in the carbon products formed over Ni-Cr-Co and Fe-Ni-Co catalysts after reacting at 450 °C. The intensity ratio, I_D/I_G, which is commonly used to estimate the defect density, was measured to be ~1.5 for these samples. This suggests a high concentration of structural defects and disordered carbon domains.

In contrast, the Co sample showed a low I_D/I_G ratio of 0.45, which can be attributed to the formation of a more ordered graphitic structure. The 2D band was also sharper and blue-shifted for the Co sample, as opposed to the broader, red-shifted 2D bands of the Ni-Cr-Co and Fe-Ni-Co samples. This confirms a higher degree of graphitization in the former.

Beyond confirming the presence of different carbon structures, Raman spectroscopy provides an important link between the structural evolution of carbon and its oxidation behavior observed by TGA. In particular, the progressive decrease of the I_D/I_G ratio and the sharpening of the 2D band with increasing reaction temperature closely mirror the systematic shift of both low- and high-temperature oxidation peaks toward higher temperatures in the DTG profiles. Similar temperature-dependent decreases in the I_D/I_G ratio during methane decomposition over Ni-based and bimetallic catalysts have been previously reported, and were attributed to progressive ordering and graphitization of the carbon products [60]. Since higher oxidation temperatures are commonly associated with increased structural order, this parallel evolution indicates that the temperature-induced ordering affects not only nanostructured carbon (e.g., nanotubes), but also surface-bound or encapsulating carbon species.

A systematic evolution of carbon structure with reaction temperature

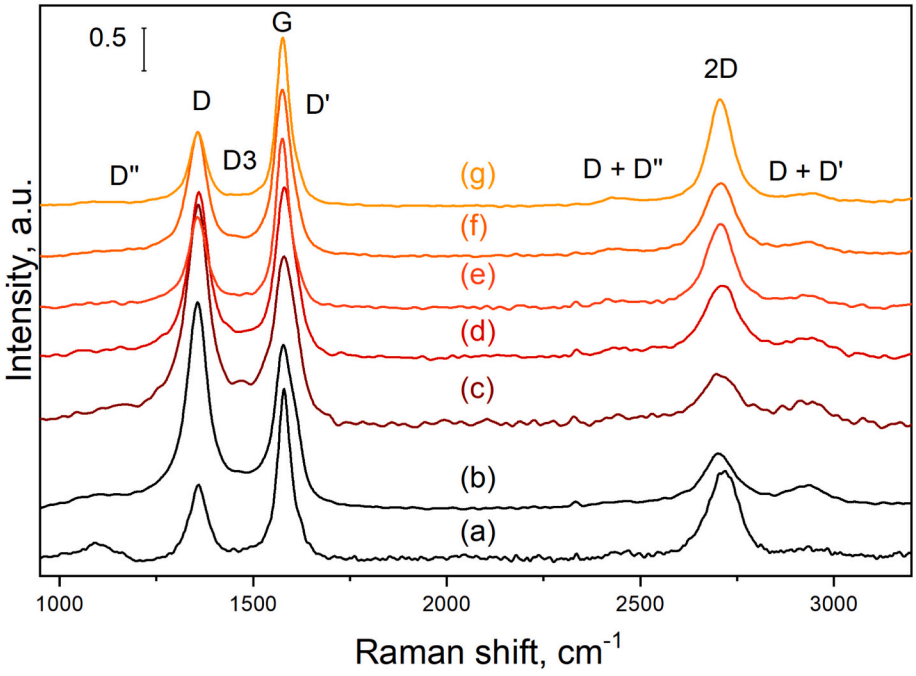

Fig. 8. Raman spectra (normalized to the G-band intensity) of the used catalysts after 10 h in methane decomposition at various temperatures: (a) Co after 550 °C; (b) Ni-Cr-Co at 450 °C; (c) Fe-Ni-Co at 450 °C; (d) Fe-Ni-Co after 500 °C; (e) Fe-Ni-Co at 550 °C; (f) Fe-Ni-Co at 600 °C; (g) Fe-Ni-Co at 650 °C;

Table 5
Parameters (the frequencies, full width at half maximum, intensity ratios) derived from Raman spectra deconvolution for all studied catalysts.

	D band, cm^{-1}		G band, cm^{-1}		I_D/I_G	I_{2D}/I_G	2D band, cm^{-1}	
	ω	FWHM	ω	FWHM			ω	FWHM
CoAl550	1358	52	1580	40	0.45	0.54	2718	95
NiCrCoAl450	1356	69	1576	51	1.44	0.40	2701	111
FeNiCoAl450	1356	72	1578	58	1.58	0.38	2705	117
FeNiCoAl500	1359	62	1578	51	1.01	0.45	2710	114
FeNiCoAl550	1356	57	1575	40	0.55	0.51	2707	88
FeNiCoAl600	1355	61	1575	49	0.76	0.46	2709	92
FeNiCoAl650	1357	54	1576	38	0.44	0.65	2706	79
Ni-Fe/SiO_2[a]	1336	–	1570	–	*0.83-1.26*	–	–	–
Ni-Co/SiO_2[a]	1336	–	1570	–	*0.77-1.08*	–	–	–
Fe-Co/SiO_2[a]	1336	–	1570	–	*0.90-1.04*	–	–	–
Ni@MC500[b]	–	–	–	–	*0.60–1.98*	0.92–0.98	2688–2714	–
Pd@MC500[b]	–	–	–	–	*0.64*	3.26	–	–
Plasma[c]	1350	–	1600	–	*6.91*	0.85	–	–

[a] *adapted from* [38]
[b] *adapted from* [22]
[c] *adapted from* [20].

is observed for the Fe-Ni-Co catalyst. Increasing the reaction temperature from 450 to 650 °C leads to a continuous decrease in the I_D/I_G ratio (from 1.58 to 0.44), suppression of defect-related bands (D′ and D3), and a pronounced increase in the intensity and sharpness of the 2D band. These changes indicate a gradual transformation from highly defective and amorphous carbon toward more ordered graphitic structures. Importantly, this Raman-derived trend is fully consistent with the TGA results, where both oxidation features shift toward higher temperatures as the reaction temperature increases, reflecting progressive structural ordering of both nanostructured and surface-confined carbon species.

Kutteri et al. [38] report characteristic Raman signatures for CNTs grown over Ni-Fe and related bimetallic catalysts operated at 650 °C under conventional thermal heating. In those systems, the I_D/I_G ratio at 650 °C lies in the range of approximately 0.77–1.26, indicating the presence of graphitic domains coexisting with a substantial density of defects. Similar values are commonly reported for oxide-supported Ni-, Fe-, and Co-based catalysts under conventional heating, where filamentous carbon forms but retains significant structural disorder due to defect-rich growth and partial encapsulation phenomena.

For microwave-heated CDM the similar products structural disorder was reported. For example, Pd@MC500 under microwave heating [22] exhibits an I_D/I_G ratio of 0.64, suggesting moderately ordered graphitic carbon, though still significantly more defective than the graphitic structures obtained over Fe-Ni-Co catalyst in the present work. In contrast, plasma-based methane decomposition [20] yields to formation of carbon structures with markedly different Raman characteristics, with a very high I_D/I_G value (~6.9), consistent with highly defective, disordered carbon such as carbon black rather than well-developed graphitic nanostructures.

Against this broader benchmark, the Fe-Ni-Co catalyst investigated in this work (55Fe-28Ni-17Co) leads to formation of less defective carbon structures. This is supported by Raman spectra of the products which exhibits an I_D/I_G value of 0.44 at 650 °C, substantially lower than the one for conventionally heated Ni-Fe systems and microwave-assisted Pd-based systems reported at similar temperatures. Together with the pronounced and sharpened 2D band, this indicates a higher degree of graphitic ordering under magnetic induction heating.

4. Conclusion

In this work, we demonstrated for the first time the experimental feasibility of catalytic methane decomposition enabled by magnetic induction heating. Magnetic nanoparticles based on Co, Fe-Cr-Co, Ni-Cr-Co and Fe-Ni-Co alloys were evaluated in the 450–650 °C range, revealing composition- and temperature-dependent catalytic behavior and distinct carbon formation pathways.

Among the tested materials, the Fe-Ni-Co alloy exhibited the highest stability and sustained methane conversion exceeding 40% at 650 °C, with no observable deactivation after 10 h of operation. Importantly, the magnetic induction heating regime appears to play a central role in stabilizing catalytic performance, suggesting localized nanoparticle heating and a different mechanism of heat and mass transfer compared to conventionally heated systems.

A systematic transition in carbon morphology with reaction temperature increase was observed. At temperatures below 550 °C, carbon nanotubes and nanofibers are the main products, whereas at higher temperatures, more ordered graphitic layers form directly on the catalyst surface. Despite the development of graphitic surface layers, no catalytic inhibition was detected, indicating that methane decomposition can proceed either through partial diffusion across carbon layers or via persistent activity at metal-carbon interfaces.

The evolution toward more ordered carbon structures at elevated temperatures was consistently confirmed by TGA oxidation profiles, Raman spectroscopy, and electron microscopy. These findings establish magnetic induction heating applied for CDM is a promising electrification path that enables controlled methane decomposition and tunable nanostructured carbon formation, opening new opportunities for methane and biogas recycling.

CRediT authorship contribution statement

Sergey Girshevich: Writing – original draft, Visualization, Validation, Methodology, Investigation, Formal analysis, Data curation, Conceptualization. **Stanislav Yakushkin:** Writing – review & editing, Supervision, Software, Project administration, Methodology, Conceptualization. **Saso Gyergyek:** Writing – review & editing, Investigation, Formal analysis. **Janvit Teržan:** Writing – review & editing, Supervision, Methodology, Conceptualization. **Anja Sedminek:** Writing – review & editing, Investigation, Formal analysis. **Anej Blažič:** Writing – review & editing, Investigation, Formal analysis. **Elena Sutormina:** Writing – review & editing, Formal analysis. **Ilja Gasan Osojnik Črnivec:** Writing – review & editing, Resources, Project administration, Funding acquisition. **Blaž Likozar:** Writing – review & editing, Supervision, Resources, Project administration, Funding acquisition, Conceptualization.

Declaration of competing interest

The authors declare the following financial interests/personal relationships which may be considered as potential competing interests:

Blaz Likozar reports financial support was provided by European Research Council. David Bajec reports financial support was provided by Slovenian Research and Innovation Agency. Saso Gyergyek reports financial support was provided by Slovenian Research and Innovation Agency. If there are other authors, they declare that they have no known competing financial interests or personal relationships that could have appeared to influence the work reported in this paper.

Acknowledgements

This work was supported by the European Research Council under the STORMING project (grant agreement no. 101069690), e-CODUCT project (grant agreement no. 101058100) and TEMPEST project (grant agreement no. 101103681), and the European Union NextGenerationEU through project HyBReED. Special thanks go to all the staff of the Department of Catalysis and Chemical Reaction Engineering at National Institute of Chemistry for their support and assistance throughout this paper, especially Katja Vodlan, Urška Kavčič and Simon Starašinič. SG acknowledges the financial support from the Slovenian Research Agency (research core funding No. P2–0089) and the access to research equipment via ARIS program P1-0417 and project Z2-50049. We acknowledge the CENN Nanocenter for the use of the Raman spectrometer NT-MDT model Integra Spectra for Materials Science and Damjan Vengust for acquiring spectra. The authors are also grateful for the funding that was provided by the European Research Council and Slovenian Research and Innovation Agency.

Appendix A. Supplementary data

Supplementary data to this article can be found online at https://doi.org/10.1016/j.cej.2026.175063.

Data availability

Data will be made available on request.

References

[1] Z. Vacek, S. Vacek, J. Cukor, European forests under global climate change: review of tree growth processes, crises and management strategies, J. Environ. Manag. 332 (2023), https://doi.org/10.1016/j.jenvman.2023.117353.
[2] E. Gsottbauer, M. Kirchler, C. König-Kersting, Financial professionals and climate experts have diverging perspectives on climate action, Commun. Earth Environ. 5 (2024), https://doi.org/10.1038/s43247-024-01331-9.
[3] E.L. Lawrance, R. Thompson, J. Newberry Le Vay, L. Page, N. Jennings, The impact of climate change on mental health and emotional wellbeing: a narrative review of current evidence, and its implications, Int. Rev. Psychiatry 34 (2022) 443–498, https://doi.org/10.1080/09540261.2022.2128725.
[4] S. Evro, B.A. Oni, O.S. Tomomewo, Carbon neutrality and hydrogen energy systems, Int. J. Hydrog. Energy 78 (2024) 1449–1467, https://doi.org/10.1016/j.ijhydene.2024.06.407.
[5] International Energy Agency, Global Hydrogen Review 2024, Glob. Hydrog. Rev. 2024 (2024), https://doi.org/10.1787/cb2635f6-en.
[6] H. Ishaq, I. Dincer, C. Crawford, A review on hydrogen production and utilization: challenges and opportunities, Int. J. Hydrog. Energy 47 (2022) 26238–26264, https://doi.org/10.1016/j.ijhydene.2021.11.149.
[7] A.L. Moghaddam, S. Hejazi, M. Fattahi, M.G. Kibria, M.J. Thomson, R. AlEisa, M. A. Khan, Methane pyrolysis for hydrogen production: navigating the path to a net zero future, Energy Environ. Sci. (2025) 2747–2790, https://doi.org/10.1039/d4ee06191h.
[8] J. Riley, C. Atallah, R. Siriwardane, R. Stevens, Technoeconomic analysis for hydrogen and carbon co-production via catalytic pyrolysis of methane, Int. J. Hydrog. Energy 46 (2021) 20338–20358, https://doi.org/10.1016/j.ijhydene.2021.03.151.
[9] S.B. Portillo, M. Kosari, F. Li, Supported transition metals for catalytic decomposition of methane: advances, Challenges, and Outlook, 2026, https://doi.org/10.1021/acscatal.5c07379.
[10] J.A. Lopez-ruiz, Y. Jiang, N.W. Riedel, R.S. Weber, C. Jiang, M. Xu, J. Hu, R. A. Dagle, CO 2 -free (turquoise) H 2 at $ 1 / kg via thermocatalytic decomposition of methane and sale of solid carbon co-product. An experimental and techno-economic analysis, Int. J. Hydrog. Energy 207 (2026) 153492, https://doi.org/10.1016/j.ijhydene.2026.153492.
[11] E. Välimäki, L. Yli-Varo, H. Romar, U. Lassi, Carbons formed in methane thermal and thermocatalytic decomposition processes: properties and applications, C 7 (2021) 50, https://doi.org/10.3390/c7030050.
[12] N.Z. Muradov, T.N. Veziroğlu, From hydrocarbon to hydrogen-carbon to hydrogen economy, Int. J. Hydrog. Energy 30 (2005) 225–237, https://doi.org/10.1016/j.ijhydene.2004.03.033.
[13] M. Xu, J.A. Lopez-ruiz, L. Kovarik, M.E. Bowden, S.D. Davidson, R.S. Weber, I. Wang, J. Hu, R.A. Dagle, Applied Catalysis A, General Structure sensitivity and its effect on methane turnover and carbon co-product selectivity in thermocatalytic decomposition of methane over supported Ni catalysts, Appl. Catal. A, Gen. 611 (2021) 117967, https://doi.org/10.1016/j.apcata.2020.117967.
[14] S. Sakthivel, Perspectives on CO2-free hydrogen production: insights and strategic approaches, Energy Fuel (2024), https://doi.org/10.1021/acs.energyfuels.4c03156.
[15] Y. Chen, B. Robinson, C. Jiang, B.K. Desta, Y. Wang, C.E. Dumitrescu, D. Bhattacharyya, J. Hu, Improved Efficiency of CO 2 Conversion to Olefins in a Thermal – Microwave Hybrid Heating Reactor, 2025, https://doi.org/10.1021/acssuschemeng.5c01387.
[16] S. Li, W.C. Wilfong, Q. Wang, Y. Chen, C. Jiang, M. Stuckman, Y. Tang, J. Hu, F. Shi, Recent Advances and Future Perspectives of Low-Concentration CO 2 Enrichment and Emerging Applications, 2025, https://doi.org/10.1021/acs.energyfuels.5c03490.
[17] S. Girshevich, D. Bajec, S. Yakushkin, J. Teržan, B. Likozar, Electrification of catalytic methane decomposition to hydrogen and nanostructured carbonaceous materials, Int. J. Hydrog. Energy 160 (2025), https://doi.org/10.1016/j.ijhydene.2025.150466.
[18] S.R. Patlolla, K. Katsu, A. Sharafian, K. Wei, O.E. Herrera, W. Mérida, A review of methane pyrolysis technologies for hydrogen production, Renew. Sust. Energ. Rev. 181 (2023), https://doi.org/10.1016/j.rser.2023.113323.
[19] S. Wang, S. Sun, D. Feng, J. Chen, G. Wang, Q. Shang, Plasma-catalytic methane decomposition : radical-mediated pathways and controlled CNTs growth over plasma-modified Fe catalyst, J. Anal. Appl. Pyrolysis 194 (2026).
[20] F. Cepeda, L. Di Liddo, L. Mendoza, M.J. Thomson, Plasma-enhanced microwave-driven methane pyrolysis for hydrogen and carbon production, J. Energy Inst. 124 (2026) 102400, https://doi.org/10.1016/j.joei.2025.102400.
[21] Y. Shen, Microwave-driven catalytic pyrolysis and reforming of methane for hydrogen production, Green Chem. (2026) 1346–1374, https://doi.org/10.1039/d5gc04777c.
[22] R.C. Seyfeli, D. Varisli, Microwave assisted methane decomposition reaction using nickel-palladium catalysts supported on different carbon supports, Int. J. Hydrog. Energy 190 (2025) 152076, https://doi.org/10.1016/j.ijhydene.2025.152076.
[23] L. Truong-Phuoc, C. Duong-Viet, J.M. Nhut, A. Pappa, S. Zafeiratos, C. Pham-Huu, Induction heating for the electrification of catalytic processes, ChemSusChem (2025) 202402335, https://doi.org/10.1002/cssc.202402335.
[24] L. Truong-phuoc, A. Essyed, X. Pham, T. Romero, J. Dath, Catalytic methane decomposition process on carbon-based catalyst under contactless induction, 2024, https://doi.org/10.20517/cs.2024.50.
[25] L. Fulcheri, V.J. Rohani, E. Wyse, N. Hardman, E. Dames, An energy-efficient plasma methane pyrolysis process for high yields of carbon black and hydrogen, Int. J. Hydrog. Energy 48 (2023) 2920–2928, https://doi.org/10.1016/j.ijhydene.2022.10.144.
[26] C. Jiang, I.W. Wang, X. Bai, S. Balyan, B. Robinson, J. Hu, W. Li, A. Deibel, X. Liu, F. Li, L.M. Neal, J. Dou, Y. Jiang, R. Dagle, J.A. Lopez-Ruiz, G. Skoptsov, Methane catalytic pyrolysis by microwave and thermal heating over carbon nanotube-supported catalysts: productivity, kinetics, and energy efficiency, Ind. Eng. Chem. Res. 61 (2022) 5080–5092, https://doi.org/10.1021/acs.iecr.1c05082.
[27] A. Deibel, S. Balyan, X. Zhu, C. Jiang, W. Li, J. Hu, X. Liu, Surface exsolving perovskite ceramics as catalyst for microwave methane pyrolysis to co-generate hydrogen and carbon nanotube, Int. J. Hydrog. Energy 69 (2024) 874–882, https://doi.org/10.1016/j.ijhydene.2024.05.052.
[28] A. Essyed, X.H. Pham, L. Truong-Phuoc, T. Romero, J.M. Nhut, C. Duong-Viet, A. Brazier, L. Vidal, J.P. Dath, M. Dumont, C. Pham-Huu, High-efficiency graphene-coated macroscopic composite for catalytic methane decomposition operated with induction heating, Chem. Eng. J. 485 (2024) 150006, https://doi.org/10.1016/j.cej.2024.150006.
[29] R.E. Rosensweig, Heating magnetic fluid with alternating magnetic field, J. Magn. Magn. Mater. 252 (2002) 370–374, https://doi.org/10.1016/S0304-8853(02)00706-0.
[30] S. Ceylan, C. Friese, C. Lammel, K. Mazac, A. Kirschning, Inductive heating for organic synthesis by using functionalized magnetic nanoparticles inside microreactors, Angew. Chem. Int. Ed. 47 (2008) 8950–8953, https://doi.org/10.1002/anie.200801474.
[31] J.S. Pavelić, S. Gyergyek, B. Likozar, M. Grilc, Process electrification by magnetic heating of catalyst, Chem. Eng. J. 505 (2025), https://doi.org/10.1016/j.cej.2024.158928.
[32] J. Marbaix, N. Mille, L.M. Lacroix, J.M. Asensio, P.F. Fazzini, K. Soulantica, J. Carrey, B. Chaudret, Tuning the composition of FeCo nanoparticle heating agents for magnetically induced catalysis, ACS Appl. Nano Mater. 3 (2020) 3767–3778, https://doi.org/10.1021/acsanm.0c00444.
[33] L.M. Martínez-Prieto, J. Marbaix, J.M. Asensio, C. Cerezo-Navarrete, P.F. Fazzini, K. Soulantica, B. Chaudret, A. Corma, Ultrastable magnetic nanoparticles encapsulated in carbon for magnetically induced catalysis, ACS Appl. Nano Mater. 3 (2020) 7076–7087, https://doi.org/10.1021/acsanm.0c01392.
[34] M.R. Almind, S.B. Vendelbo, M.F. Hansen, M.G. Vinum, C. Frandsen, P. M. Mortensen, J.S. Engbæk, Improving performance of induction-heated steam

methane reforming, Catal. Today 342 (2020) 13–20, https://doi.org/10.1016/j.cattod.2019.05.005.
[35] V. Poletto Dotsenko, M. Bellusci, A. Masi, D. Pietrogiacomi, F. Varsano, Improving the performances of supported NiCo catalyst for reforming of methane powered by magnetic induction, Catal. Today 418 (2023) 114049, https://doi.org/10.1016/j.cattod.2023.114049.
[36] D. Hantoko, W.U. Khan, A.I. Osman, M. Nasr, A.K. Rashwan, Y. Gambo, A. Al Shoaibi, S. Chandrasekar, M.M. Hossain, Carbon–Neutral Hydrogen Production by Catalytic Methane Decomposition: A Review, Springer International Publishing, 2024, https://doi.org/10.1007/s10311-024-01732-4.
[37] B. Gao, I.W. Wang, L. Ren, T. Haines, J. Hu, Catalytic performance and reproducibility of Ni/Al2O3 and co/Al2O3 mesoporous aerogel catalysts for methane decomposition, Ind. Eng. Chem. Res. 58 (2019) 798–807, https://doi.org/10.1021/acs.iecr.8b04223.
[38] D. Ayillath Kutteri, I.W. Wang, A. Samanta, L. Li, J. Hu, Methane decomposition to tip and base grown carbon nanotubes and COx-free H2 over mono- and bimetallic 3d transition metal catalysts, Cat. Sci. Technol. 8 (2018) 858–869, https://doi.org/10.1039/c7cy01927k.
[39] M. Pudukudy, Z. Yaakob, M.Z. Mazuki, M.S. Takriff, S.S. Jahaya, One-pot sol-gel synthesis of MgO nanoparticles supported nickel and iron catalysts for undiluted methane decomposition into COx free hydrogen and nanocarbon, Appl. Catal. B Environ. 218 (2017) 298–316, https://doi.org/10.1016/j.apcatb.2017.04.070.
[40] N. Bayat, M. Rezaei, F. Meshkani, Methane decomposition over Ni-Fe/Al2O3 catalysts for production of COx-free hydrogen and carbon nanofiber, Int. J. Hydrog. Energy 41 (2016) 1574–1584, https://doi.org/10.1016/j.ijhydene.2015.10.053.
[41] N. Bayat, F. Meshkani, M. Rezaei, Thermocatalytic decomposition of methane to COx-free hydrogen and carbon over Ni-Fe-cu/Al2O3 catalysts, Int. J. Hydrog. Energy 41 (2016) 13039–13049, https://doi.org/10.1016/j.ijhydene.2016.05.230.
[42] D. Torres, J.L. Pinilla, I. Suelves, Cobalt doping of α-Fe/Al2O3 catalysts for the production of hydrogen and high-quality carbon nanotubes by thermal decomposition of methane, Int. J. Hydrog. Energy 45 (2020) 19313–19323, https://doi.org/10.1016/j.ijhydene.2020.05.104.
[43] A.H. Fakeeha, A.A. Ibrahim, W.U. Khan, K. Seshan, R.L. Al Otaibi, A.S. Al-Fatesh, Hydrogen production via catalytic methane decomposition over alumina supported iron catalyst, Arab. J. Chem. 11 (2018) 405–414, https://doi.org/10.1016/j.arabjc.2016.06.012.
[44] A.S. Al-Fatesh, A.H. Fakeeha, W.U. Khan, A.A. Ibrahim, S. He, K. Seshan, Production of hydrogen by catalytic methane decomposition over alumina supported mono-, bi- and tri-metallic catalysts, Int. J. Hydrog. Energy 41 (2016) 22932–22940, https://doi.org/10.1016/j.ijhydene.2016.09.027.
[45] Ž. Ponikvar, A. Sedminek, J. Teržan, L. Skubic, Ž. Lavrič, M. Huš, M. Grilc, B. Likozar, D. Makovec, S. Gyergyek, Electrified Dynamically Responsive Ammonia Decomposition to Hydrogen Based on Magnetic Heating of a Ru Nanocatalyst, ChemSusChem 202401970 (2024) 1–11, https://doi.org/10.1002/cssc.202401970.
[46] M. Wojdyr, Fityk: a general-purpose peak fitting program, J. Appl. Crystallogr. 43 (2010) 1126–1128, https://doi.org/10.1107/S0021889810030499.
[47] Naresh Shah, Devadas Panjala, Gerald P. Huffman, Hydrogen Production by Catalytic Decomposition ofMethane, Energy & Fuels (2001) 1520–5029, https://doi.org/10.1021/ef0101964.
[48] D. Hantoko, W.U. Khan, A.I. Osman, M. Nasr, A.K. Rashwan, Y. Gambo, A. Al Shoaibi, S. Chandrasekar, M.M. Hossain, Carbon–Neutral Hydrogen Production by Catalytic Methane Decomposition: A Review, Springer International Publishing, 2024, https://doi.org/10.1007/s10311-024-01732-4.
[49] N. Bayat, M. Rezaei, F. Meshkani, Hydrogen and carbon nanofibers synthesis by methane decomposition over Ni e Pd / Al 2 O 3 catalyst, Int. J. Hydrog. Energy 41 (2016) 5494–5503, https://doi.org/10.1016/j.ijhydene.2016.01.134.
[50] M. Stückler, H. Krenn, R. Pippan, L. Weissitsch, S. Wurster, A. Bachmaier, Magnetic binary supersaturated solid solutions processed by severe plastic deformation, Nanomaterials 9 (2019) 1–8, https://doi.org/10.3390/nano9010006.
[51] A. Sedminek, D. Makovec, J. Teržan, B. Likozar, P. Jenuš, A. Kocjan, G. Marolt, S. Gyergyek, Scalable method for the preparation of CoxNi1-x/alumina nanocomposites and their magnetic heating properties, J. Alloys Compd. 1005 (2024), https://doi.org/10.1016/j.jallcom.2024.176109.
[52] N.M. and S.K. Rapolu Sridhar, D. Ravinder, J. Laxman Naik, K. Vijaya Kumar, Investigation of structural, magnetic and electrical properties of chromium substituted nickel ceramic Nanopowders, Adv. Ceram. Mater. (2020), https://doi.org/10.5772/intechopen.94941.
[53] M.J. Besnus, Y. Gottehrer, G. Munschy, Magnetic properties of NiCr alloys, Phys. Status Solidi 49 (1972) 597–607, https://doi.org/10.1002/pssb.2220490222.
[54] J. Guo, H. Lou, X. Zheng, The deposition of coke from methane on a Ni/MgAl2O4 catalyst, Carbon N. Y. 45 (2007) 1314–1321, https://doi.org/10.1016/j.carbon.2007.01.011.
[55] X. Jia, L. Zhang, J. Jia, A. Zhou, Formation and reactivity of surface carbonaceous species from ethylene decomposition on Ni-based catalyst treated using dielectric barrier discharge plasma, Appl. Catal. A Gen. 669 (2024) 119510, https://doi.org/10.1016/j.apcata.2023.119510.
[56] Y. Ren, Y.Y. Ma, W.L. Mo, J. Guo, Q. Liu, X. Fan, S.P. Zhang, Research Progress of carbon deposition on Ni-based catalyst for CO2-CH4 reforming, Catalysts 13 (2023), https://doi.org/10.3390/catal13040647.
[57] I.W. Wang, D.A. Kutteri, B. Gao, H. Tian, J. Hu, Methane pyrolysis for carbon nanotubes and CO x -free H 2 over transition-metal catalysts, Energy Fuel 33 (2019) 197–205, https://doi.org/10.1021/acs.energyfuels.8b03502.
[58] B. Gao, I.W. Wang, L. Ren, J. Hu, Catalytic methane decomposition over bimetallic transition metals supported on composite aerogel, Energy Fuel 33 (2019) 9099–9106, https://doi.org/10.1021/acs.energyfuels.9b01723.
[59] I. Wang, R.A. Dagle, T.S. Khan, J.A. Lopez-Ruiz, L. Kovarik, Y. Jiang, M. Xu, Y. Wang, C. Jiang, S.D. Davidson, P. Tavadze, L. Li, J. Hu, Catalytic decomposition of methane into hydrogen and high-value carbons: combined experimental and DFT computational study, Catal, Sci. Technol. 11 (2021) 4911–4921, https://doi.org/10.1039/d1cy00287b.
[60] M. Xu, J.A. Lopez-Rui, N.W. Riedel, R.S. Weber, M.E. Bowden, L. Kovarik, C. Jiang, J. Hu, R.A. Dagle, Promotional role of NiCu alloy in catalytic performance and carbon properties for CO2-free H2 production from thermocatalytic decomposition of methane, Cat. Sci. Technol. (2023), https://doi.org/10.1039/d2cy01782b.